Gemini surfactant mediated catansomes for enhanced singlet oxygen generation of Rose Bengal and their phototoxicity against cancer cells

Bunty Sharma[a,b], Mario Samperi[b,1], Akhil Jain[c], Ganga Ram Chaudhary[a], Gurpreet Kaur[a*] and Lluïsa Pérez-García[b,d,e*]

[a] Department of Chemistry, Centre for Advanced Studies in Chemistry, Panjab University, Chandigarh-160014, India

[b] Division of Advanced Materials and Healthcare Technologies, School of Pharmacy, University of Nottingham, Nottingham NG7 2RD, UK

[c] Division of Regenerative Medicine and Cellular Therapies, School of Pharmacy, University of Nottingham, Nottingham NG7 2RD, UK

[d] Departament de Farmacologia, Toxicologia i Química Terapèutica, Facultat de Farmàcia i Ciències de l'Alimentació, Avda. Joan XXIII 27-31, Universitat de Barcelona, 08028 Barcelona, Spain

[e] Institut de Nanociència i Nanotecnologia UB (IN2UB), Universitat de Barcelona, 08028 Barcelona, Spain

*corresponding authors: Lluïsa Pérez-García (email: mlperez@ub.edu)

Gurpreet Kaur (e-mail: gurpreet14@pu.ac.in)

[1] Present address: Istituto di Tecnologie Avanzate per l'Energia "Nicola Giordano" - CNR-ITAE, Messina, Italy

Abstract- Photodynamic therapy (PDT) is a innovative technique for cancer treatment with minimal side effects, based on the use of a photosensitizer, oxygen, and light. Photosensitizers (PS) have several limitations that may limit their clinical practice, like poor solubilization, self-aggregation, and lack of specific targeting, that can be addressed with the use of nanomaterials. Herein, a unique type of catansomes (CaS) was prepared using a gemini imidazolium-based surfactant (1,3-bis[(3-octadecyl-1-imidazolio)methyl]benzene dibromide (GBIB) and a double chain diaoctyl sodium sulfosuccinate or Aerosol OT (AOT). The formation of catansomes GBIB:AOT was optimized in various ethanol:water (E:W) solvent ratios employing a facile, quick and most reliable solution-solution mixing method. CaS were characterized by dynamic light scattering (DLS) and field emission gun-scanning electron microscopy (FEG-SEM) techniques. The experimental results reveal that stable CaS were obtained at lower concentrations (100 µM) with a spherical shape. Rose Bengal (RB), a PS of the xanthene´s family, was incorporated into these prepared CaS, as proved by fluorescence spectroscopy, UV-visible absorption spectroscopy, and confocal laser scanning microscopy. Singlet oxygen ($^1O_2$) generation studies reveal the relevant role of the E:W solvent ratio from RB encapsulated in CaS, since there was a 4-fold boost in the $^1O_2$ production for GBIB:AOT in E:W (50:50) and around 3-fold in E:W (30:70). Also, the GBIB rich (80:20) fraction was more efficient in increasing the $^1O_2$ generation as compared to AOT rich fraction (20:80), and their phototoxicity was tested, in water-rich solvent ratio E:W (30:70), against MCF-7 cells. Upon irradiation with a 532 nm laser (50 mW), this RB-loaded CaS showed a significant decrease in the metabolic activity of MCF-7 cells, and RB@GBIB:AOT(80:20) fraction showed a maximum 85 % decrease in cell viability. Furthermore, the enhancement in intracellular $^1O_2$ generation by RB@GBIB:AOT, as compared to pure RB, was confirmed by the singlet oxygen sensor green (SOSG). This new type of catansomes based on gemini surfactants exhibiting a large amount of $^1O_2$ generation of great interest for several applications, as in photomedicine.

Keywords: Catansomes, Catanionic, Ethosomes, Vesicles, Singlet Oxygen, Rose Bengal, Phototoxicity

Introduction: Singlet oxygen ($^1O_2$) is the lowest excited state of molecular oxygen, and generates highly toxic reactive oxygen species (ROS), which study is important in the fields of medicine, biology or materials science and shows high importance in biomedical applications. It is also used for treating unwanted species like cancer cells, bacterial biofilms, and fungs. It can harm biomolecules nucleic acid, proteins, lipids and is assumed to have a deleterious effect on cancer cells. There are different photosensitizers (PSs) investigated for $^1O_2$ generation study and few of them were FDA approved [1-3]. $^1O_2$ is generated upon energy transmission from the excited triplet state of photosensitizer (PS^3) to the molecular oxygen (triplet state oxygen in the ground state) [4]. This $^1O_2$ generation process effected by the environment of PS. For example, incorporation of indocyanine green (ICG) a PS into thermal responsive liposome resulted in an increase in photodynamic therapy (PDT) efficacy [5]. PDT depends on the interaction between PS, light, and ground-state molecular oxygen [6]. PS is triggered by a specific wavelength of light and directly goes to an excited triplet state by inter-system conversion and then reacts with molecular oxygen in the triplet state. Due to charge transfer from the excited state of PS (triplet state), oxygen gets converted into $^1O_2$ which is highly toxic [7-10]. Recently, scientists have also proposed the role of $^1O_2$ against the killing of SARS-COVID-19 by PDT [11,12].

$^1O_2$ generation using PS depends on different factors like the type of PS, concentration, pH, solvent polarity [13]. There are several reports on $^1O_2$ generation in pure solvents like water, ethanol but there are few studies on the use of a mixture for this purpose. Effective photosensitizing drug delivery to the cancer cell is a great concern for an efficient photodynamic effect by increase the drug loading and $^1O_2$ yield [14,15]. There is a need to design new ideal nanosized PSs delivery agents which can effectively deliver PS to the tumor

site [16]. A variety of PS carriers have been investigated such as metal-organic framework, and biopolymer micro/nanoparticles but these carriers required a complicated long synthetic procedure [17,18]. In literature, there are very few reports in which a mixture of solvent was used for delivery system and studied in PDT. Souza et al. studied the peptide-based self-assembly in ethanol:water (E:W) 1:1 for singlet oxygen generations [19]. Kessel and co-workers have also examined the tin etiopurpurin ($SnET_2$) ethanol-soluble drug delivery through water-soluble cyclodextrin derivate as delivering agent [20].

One particular interesting drug delivery system is organic supramolecular entities containing phospholipids. The vesicles constructed from phospholipids using an ethanol-water mixture are known as "Ethosomes". Ethosomes are the well-known non-invasive soft malleable systems for dermal and transdermal drugs delivery of molecules and have improved skin penetration effect, due to the presence of ethanol content [21,22]. It is a rapidly growing field and its commercialization started in 2000 [23]. The vesicles formed by mixing oppositely charged surfactant in a non-equimolar ratio without the input of external energy are known as "Catanionic vesicles" [24-26]. Sarma et al. prepared 30/70 ratio of cetytrimethylammonium bromide (CTAB)/sodium dodecyl sulfate (SDS) in water and then various straight chains lengths of alcohol (C_nOH) were added which confirmed that the presence of alcohol stabilizes the catanionic vesicles [27]. Cosolvent presence enhanced the stability of the catanionic vesicles [28]. The hybrid of these two types i.e. catanionic and ethosomes vesicles is known as "Catansomes" (CaS). CaS are a new type of delivery system that have not been explored for PSs delivery in PDT. To the best of our knowledge, there is no article available on gemini-based catansomes systems for PS encapsulation and in PDT.

In this work, we developed gemini based catansomes in a mixture of ethanol and water solvent at various ratios. Here we demonstrated how solvent ratio effect the self-assembly and the properties of final aggregates of double chain cationic gemini imidazolium-based surfactant

(1,3-bis[(3-octadecyl-1-imidazolio)methyl]benzene dibromide (GBIB) and a double chain diaoctyl sodium sulfosuccinate or Aerosol OT (AOT). In our previous study found that solvent ratios played an important role on aggregation behaviour of pure gemini GBIB surfactant [29,30]. These cationic GBIB and anionic double chain AOT surfactants were mixed in different molar ratios in various E:W (30:70, 50:50, and 70:30) solvent ratios. These catansomes were then characterized using dynamic light scattering (DLS), field emission gun scanning electron microscope (FEG-SEM). Rose Bengal (RB) a well-known PS was encapsulated into catansomes and were characterized using confocal laser scanning microscopy (CLSM). The chemical trapping method was used to identify the singlet oxygen generation ability of the RB encapsulated in CaS. This RB-loaded CaS mixture was evaluated against MCF-7 cancer cell lines using PDT. Scheme 1 shows the molecular structure of the cationic GBIB and anionic AOT surfactant-based CaS formation and their use in phototoxicity against cancer cells. To the best of our knowledge, this is the first study that reports on the application of catansomes for singlet oxygen-mediated phototoxicity against cancer cells.

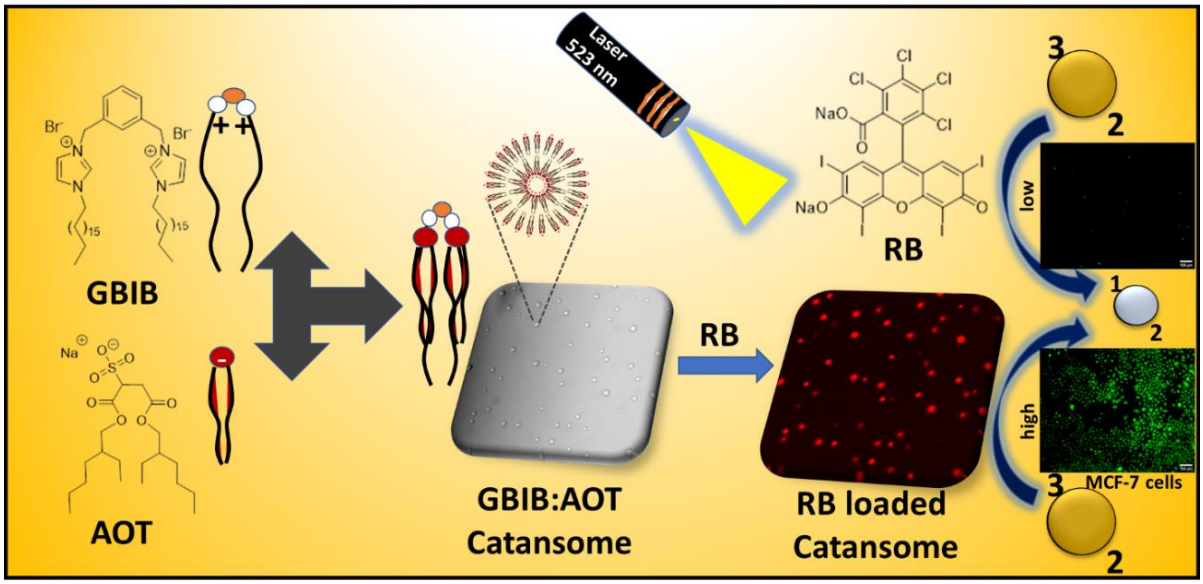

Scheme 1. Schematic illustration of the GBIB based catansomes formation and PS encapsulation which was later used for singlet oxygen generation and phototoxicity in cells.

2. Material and Methods:

2.1. Materials: A double chain cationic gemini imidazolium-based surfactant (1,3-bis[(3-octadecyl-1-imidazolio)methyl]benzene dibromide [$C_{50}H_{88}N_4Br_2$] (GBIB) was synthesized as our previously reported scheme [31]. Sodium bis(2-ethylhexyl sulfosuccinate) [$C_{20}H_{37}NaO_7S$] AOT was obtained from Fluka. Rose Bengal (RB) dye, 9,10-anthracenediyl-bis(methylene) dimalonic acid (ABMA), Cell Counting Kit-8, Dulbecco's Modified Eagle's Medium (DMEM), Singlet Oxygen Sensor Green (SOSG), 4',6-diamidine-2'-phenylinole dihydrochloride (DAPI) and *p*-formaldehyde (PFA) were purchased from Sigma Aldrich. WST-8. Mili-Q water and pure ethanol were used for all the experiments. All the chemicals used were of analytical grade and used as supplied without further purification and modification.

2.2. Methods:

2.2.1. Assembly of the catansomes: To synthesize the catansomes cationic GBIB and anionic AOT were dissolved separately in ethanol and Mili-Q water, respectively, and sonicated at 25 $^{\circ}$C for 5 minutes until completely dissolved. These solutions were then mixed in 10:90 to 90:10 molar ratios. To optimize the fabrication of CaS, in preliminary studies 10:90 to 90:10 ratios of both GBIB:AOT vis to vis E:W were varied. After obtaining the stable formulations, further experimentation was carried out at three different E:W solvent ratios i.e. (70:30), (50:50), and (30:70) using various concentrations of GBIB:AOT (1 mM, 0.5 mM and 0.1 mM total concentrations).

2.2.2. Hydrodynamic diameter: The hydrodynamic diameter (D_h) and polydispersity index (PDI) were determined using the DLS on Malvern Zetasizer Nano ZS by utilizing disposable cuvettes. Each sample was equilibrated for 120 seconds within the Zetasizer and 3 runs were completed for each ratio. In DLS, He-Ne laser of wavelength 633 nm and 4mW power scattered

light was detected at a 173° scattering angle. The stability of the CaS was examined for one month by measuring the D_h and PDI. All the measurements were run at 25ºC.

2.2.3. Zeta Potential (ζ): The zeta potential was also recorded on the Malvern Zetasizer Nano ZS instrument. ζ was measured in DTS1070 folded capillary cells by equilibrating the sample for 120 sec at a constant 25ºC temperature. Once each sample was analysed for zeta potential, the cells were washed out with deionized water and a different sample was injected using a clean syringe. Data processing was executed employing Malvern's Zetasizer software (7.13).

2.2.4. FEG-SEM: The field emission gun scanning electron microscope (FEG-SEM) JEOL 7100F was used to determine the surface morphology of the synthesized CaS at Nanoscale and Microscale Research NMRC, University of Nottingham. A fresh sample of CaS was casted on the aluminium stubs, dried overnight under vacuum, and then coated with a 5 nm thick layer of iridium. Imaging of the sample was carried out at 5 kV accelerating voltage with a working distance of 10 mm.

2.2.5. Photosensitizer encapsulation: In order to load RB into the vesicular mixture, we followed a reported protocol for RB encapsulation [32]. RB solution was added during the CaS formation and then sonicated for 5 min which was followed by shaking for 1 h. This mixture was later centrifuged at 13000 rpm and was filtered. The fluorescence intensity of the samples was measured on the CARY Eclipse spectrophotometer and the change in absorption value was measured on CARY 50 Bio UV-visible spectrometer. For the control sample, RB solution was prepared in respective E:W solvent ratios.

2.2.6. Confocal laser scanning microscopy: To determine entrapment of RB in fabricated CaS, fluorescence imaging on super-resolution Zeiss Elyra PS1 microscopy equipped with Zen 2012 acquisition and processing software was utilized. RB containing CaS mixture was equilibrated by putting the mixture on a shaker. Then, 20 μL of the RB-CaS mixture was placed

on the ethanol-washed glass slides and covered with micro coverslips to avoid any kind of contamination. The side of the coverslip was stick with adhesive to avoid any interference of air. Before the measurement of the sample on a confocal microscope, it was further dried for 1 to 2 h. The images were then analysed by ImageJ software.

2.2.7. Photosensitizer and light source: RB an anionic dye, a well-known PS, with absorption maxima around 547 nm was used for $^1O_2$. The stock solutions were prepared by dissolving 0.1 mg ml^{-1} of RB in water, ethanol, and E:W mixture and stored in dark by covering it with aluminium foil. A diode module laser with a wavelength of 532 nm was used, to determine $^1O_2$, which matches with absorption maxima of RB dye. The following specification of the laser was used during the experiment.

Table 1. Summary of the parameter used for the light source used for PDT.

Parameter	**Laser**
Wavelength (nm)	532 +/- 10
Power output (mW)	50
Dimension of the Light source	Diameter 0.8 cm
Lenses	Acrylic

2.2.8. *In situ* $^1O_2$ quantification: ABMA, a commonly used anthracene derivative was utilized as a molecular probe to confirm the $^1O_2$ generation by free RB, only CaS and RB loaded GBIB:AOT (80:20) and (20:80) fractions in three selected E:W solvent ratios. ABMA fluorescence intensity decay was quantified to check the PSs ability to generate $^1O_2$. This probe is very sensitive as in the presence of a slight amount of singlet oxygen, a significant decrease in the fluorescence intensity was detected [33,34]. Higher is the amount of singlet oxygen production more will be the decrease in the fluorescence intensity of ABMA [35]. The concentration of ABMA and RB was 2 μM and 4 μM, respectively, and were kept constant for each sample measurement. Each time, the fresh stock solution of CaS (100 μM) was prepared

and then 20 μM was used for the $^1O_2$ study with RB. Fluorescence emission spectra were recorded after 10 sec light irradiation till 180 sec. The percentage decay of ABMA confirmed the singlet oxygen generation ability of PS and PS in presence of CaS using the following equation [36].

$$\text{The maximum rate of ABMA photobleaching} = \frac{(\%\ \text{IF at t=0 sec}) - (\%\ \text{IF at t=60 sec})}{60\ \text{sec}\ X\ \text{PS}\ (\mu\text{M})} \quad (1)$$

Where IF, is the intensity of fluorescence of ABMA.

2.2.9. Cell culture: MCF-7 cells (a human breast cancer cell line) were purchased from American Type Culture Collection (ATCC, USA). These cells were cultured in high glucose Dulbecco's modified eagle's medium (DMEM) from Gibco containing 10% foetal bovine serum (FBS) with 1% penicillin/streptomycin. Cells were maintained at 37 ºC in an incubator with a humidified atmosphere containing 5% CO_2.

2.2.10. WST-8 assay- WST-8 assay (cell counting kit-8) was used to check the dark and phototoxicity of free RB, only catansomes, and RB-loaded catansomes. MCF-7 cells were seeded into a 96-well plate with a cell density of 8.5×10^3 cells/well and incubated for 24 h at 37℃. Further experiments were carried out in three sets, after incubation. Cells media was replaced with media containing free RB(2μM) (set 1), only GBIB:AOT CaS fractions (set 2) and RB loaded GBIB:AOT (20:80) and (80:20) fractions at concentrations (1, 2.5, 5, 7.5, and 10 μM) (set 3) and then incubated for 24 h. The concentration of RB was fixed at 2μM. Later, the cells containing CaS were washed twice with PBS and fresh media was further added, and cells were again incubated for 24 h. Next, the media was replaced with DMEM containing 10% WST-8 solution, further cells (in all three sets) were incubated for 3 h at 37 ℃. In the end, absorbance was recorded at 450 nm on the Tecan plate reader, and the cell metabolic activity was measured in accordance with the absorbance of untreated cells as background. All the experiments were performed in triplicate.

Similarly, to find out the phototoxicity three sets were prepared. After 24 h seeding of MCF-7 cells (8.5×10^3 cells/well), cell media was replaced with, free RB(2μM) (set 1). In set 2 only CaS and in set 3 RB@CaS(20:80) and RB@CaS(80:20) fractions of 5 and 10 μM were used. Afterward, cells were washed twice with PBS and fresh media was added (in all three sets) followed by plate irradiation using green diode laser light (wavelength 532 nm; power = 50 mW) for 5 min and again incubated for 24 h. Finally, media was replaced with DMEM containing 10% WST-8 followed by 3 h incubation. The absorbance was measured at 450 nm and the metabolic activity was determined. The absorbance reading of untreated cells was considered as a baseline correction.

To further confirm the intracellular uptake, MCF-7 cells were seeded with a cell density of 8.5×10^3 cells/well in a 96-well plate and incubated for 24 h at 37℃. After 24 h, cell media was replaced with fresh media containing free RB (2μM) or RB loaded in 10 μM GBIB:AOT (20:80) or (80:20) catansomes fractions prepared in E:W (30:70) solvent ratio. Throughout the experiment, the concentration of ethanol was maintained at less than 0.1%. After the incubation period, the media was removed, and cells were washed two times with PBS to remove loosely bound/unbounded RB-loaded CaS. Then, cells were fixed with 4% PFA for 15 min. After that, cells were washed twice by PBS and followed by staining with DAPI for 20 min. In the end, cells were washed with PBS and the nuclei and RB were imaged in a fluorescence microscope (Nikon Eclipse Ti) at 20X.

2.2.11. Intracellular $^1O_2$ generation- MCF-7 cells were cultured (5×10^3 cells/well) in 96-well black bottom plates and incubated for 24 h at 37℃ and 5% CO_2 atmosphere. Then cells media was replaced with media containing free RB (2 μM) and RB-loaded CaS (20:80) and (80:20) fractions (5 μM and 10 μM). After incubation for 24 h, cells were washed twice by PBS, and immediately media was changed with PBS solution containing 10 μM SOSG and incubated for 20 min [37,38]. Then, each well was irradiated for 5 min using a 532 nm laser diode light

source for 5 min. Immediately after irradiation, cells were washed with PBS, and then SOSG green fluorescence was captured using Nikon eclipse Ti fluorescence microscope with FITC filter.

3. Results and discussion:

3.1 Preparation and characterization of CaS: Catansomes (GBIB:AOT) were prepared by employing an easy, fast and reliable solution-solution mixing method. The chemical structure of the two-component surfactants is given in Scheme 1. GBIB (5 mM) and AOT (5 mM) were dissolved in ethanol and water, respectively since GBIB has very low solubility in water, and different E:W solvent mixtures were explored. GBIB:AOT fractions from 10:90 to 90:10 were prepared by changing the same E:W solvent ratios (from 10:90 to 90:10). Fig. 1(a) shows the picture of the prepared GBIB:AOT fractions from 10:90 to 90:10 molar ratio (left to right) keeping total concentration 1 mM, where E:W ratios were kept the same as those for GBIB:AOT. The turbidity and physical appearance of the prepared mixtures at various GBIB:AOT and E:W ratios suggested the formation of CaS. In Fig. 1(a), fractions containing more AOT (in water-rich) (10:90 to 50:50) showed more turbidity in the mixture. However, clear mixtures were obtained with GBIB and ethanol-rich fractions i.e. 60:40 to 90:10. Characterization of the CaS was initially performed by measuring their D_h, PDI, and zeta-potential of freshly prepared CaS mixtures at 25ºC which showed the fluctuation in values with change in GBIB:AOT fraction in different E:W solvent ratios. The D_h value changed abruptly with a minimum size of around 100 nm for GBIB:AOT (10:90) fractions while for 30:70, 40:60, and 50:50 fractions size was more than 1000 nm and formed fibres after 3 to 4 h. On the other hand, GBIB (in ethanol-rich) fractions have a size of around 500 nm (Fig. 1(b)). Fig. 1(c) shows the zeta-potential graph of different fractions which confirmed that both negative and positive surface charges containing CaS were formed. The zeta-potential value for the 10:90 fraction was -45 mV and reached maximum +45 mV at 50:50 fraction and then abruptly

decreased, suggesting that compensation of charge may cause precipitation and lead to the instability of the system at these ratios [39]. The parallel variation of E:W solvent ratio and GBIB:AOT fractions verified that solvent ratio plays a crucial role in CaS formation. This dicationic GBIB surfactant is well known for fast stable nanofiber formation at higher concentrations (12 mM) in 1:1 E:W solvent ratio [40]. To further study GBIB:AOT fraction we have chosen mixtures of GBIB:AOT fractions at fixed E:W solvent ratios, i.e. 70:30, 50:50, and 30:70.

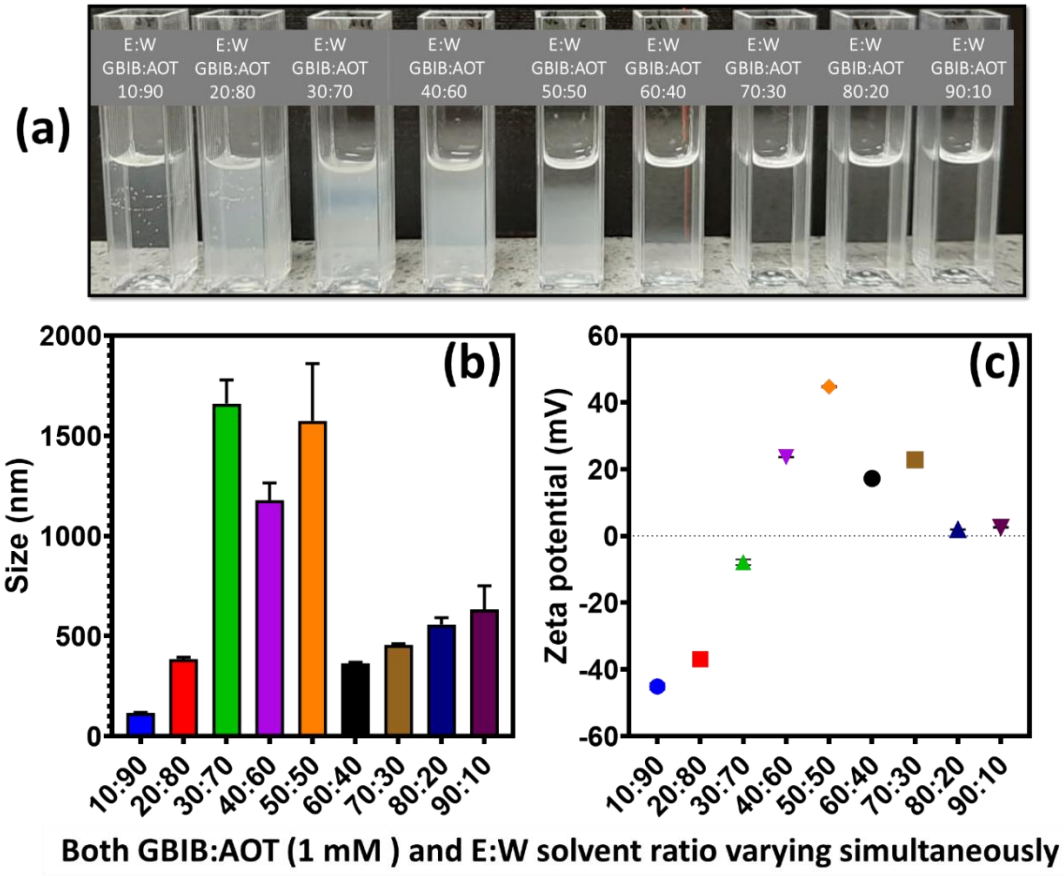

Fig. 1 CaS preparation and characterizations **(a)** Picture of the prepared GBIB:AOT (1 mM) CaS fractions in E:W solvent mixture. Both GBIB:AOT and E:W ratio alterations simultaneously from 10:90 to 90:10 (left to right) **(b)** graph of hydrodynamic diameter, determined by DLS, and **(c)** Zeta potential (mV) of the synthesized GBIB:AOT (1 mM) fractions in variable E:W mixtures.

Initially, the E:W solvent ratio was fixed to 50:50 and various fractions at three different concentrations of GBIB:AOT (1 mM, 0.5 mM, and 0.1 mM) were prepared. The picture of the prepared GBIB:AOT fractions are presented in Fig. 2(A,B,C). DLS measurements were performed for all these fractions. For 1 mM CaS concentration, 10:90 to 30:70 GBIB:AOT fractions D_h showed particle size again near 1500 nm and then continuously decreased till 90:10 fraction (Fig. 2(a)). In this case, only fluctuating positive zeta potential containing CaS were formed (Fig. 2(b)). By decreasing the total concentration of GBIB:AOT to 0.5 mM, the particle size also decreases below 1000 nm for all the fractions (Fig. 2(c)). In this case, only the 10:90 fraction has a negative charge while the other fractions have a positive zeta-potential value (Fig. 2(d)).

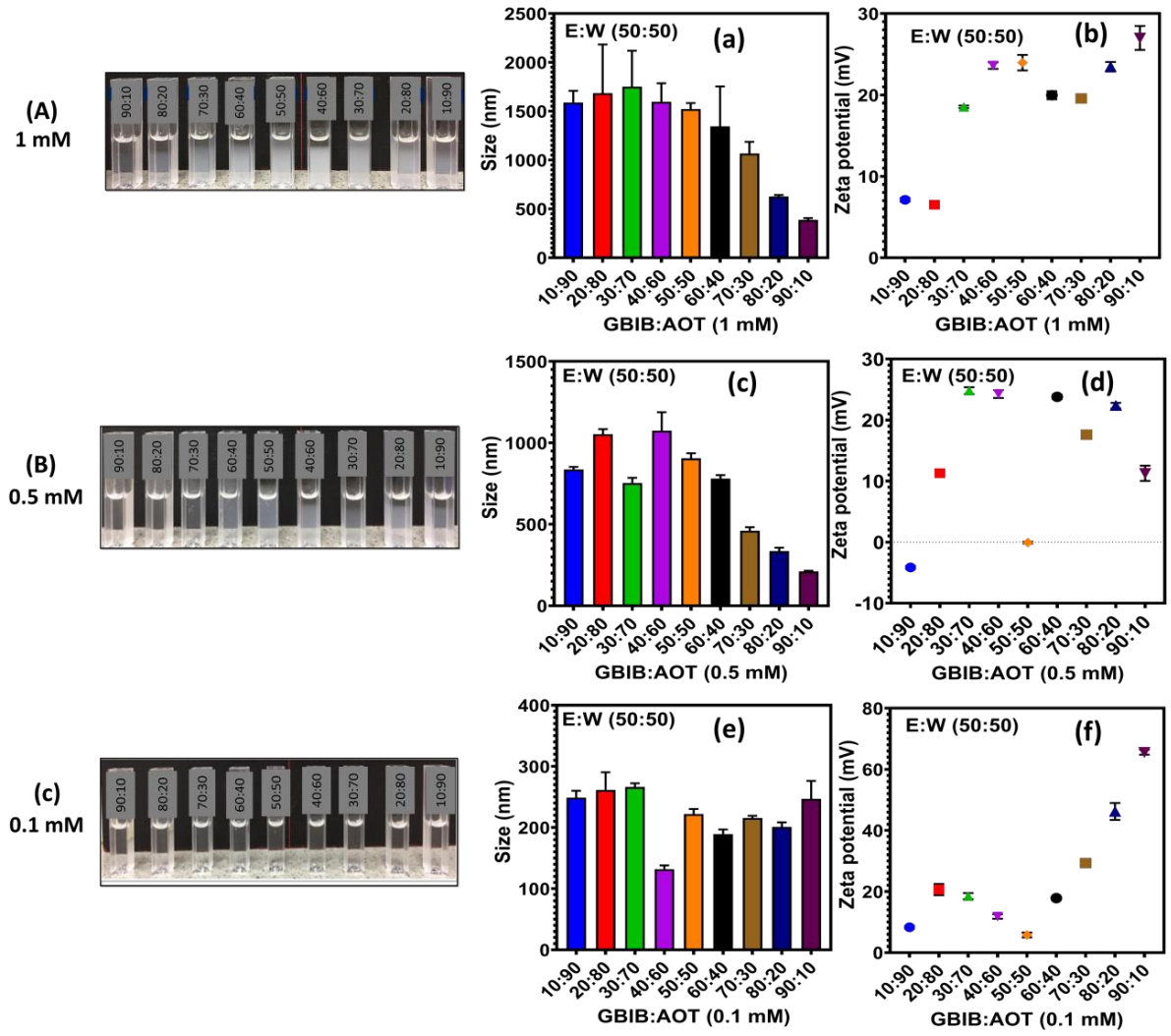

Fig. 2 Picture of the synthesised GBIB:AOT catansomes fractions. GBIB:AOT total concentration **(A)** 1 mM, **(B)** 0.5 mM and **(C)** 0.1 mM with fixed E:W (50:50) mixture. Characterization of catansomes of GBIB:AOT fractions 1 mM **(a)** hydrodynamic diameter and **(b)** zeta potential and GBIB:AOT (0.5 mM) fractions **(c)** hydrodynamic diameter and **(d)** zeta potential and GBIB:AOT (0.1 mM) fractions **(e)** hydrodynamic diameter and **(f)** zeta potential in E:W (50:50) mixture.

Instead, more uniform particle size between 100 nm to 300 nm (Fig. 2(e)) with positive zeta potential (Fig. 2(f)) were obtained when a total concentration of 0.1 mM GBIB:AOT was used. This experiment confirmed that at 50:50 E:W solvent ratio the clear dominance of GBIB locating towards the external surface side of the CaS. After two to four days, catanionic gelation occurred at 50:50 GBIB:AOT fractions of 1 mM and 0.5 mM total concentration, a result with is in concordance of the gelation ability exhibited by GBIB, at higher concentrations [40].

Out of the above-studied concentrations, a consistent size formation was observed at 0.1 mM total concentration at E:W (50:50) solvent ratio. Then, E:W (70:30) and (30:70) solvent ratios (Fig. S1(A,B)) were explored. In E:W (70:30) solvent ratio, the CaS size was between 200-500 nm, while zeta-potential was positive for all the fractions with maximum +35 mV for 70:30 fraction (Fig. 3(a)&(b)). In most of GBIB:AOT fractions in E:W(30:70) mixture, the D_h was around 200 nm and only for 10:90 and 20:80 fractions a size greater than 200 nm (Fig. 3(c)) was observed. In this case, these two fractions (10:90 and 20:80) had negative zeta-potential while other fractions had carried overall positive charge as depicted from zeta-potential measurements (Fig. 3(d)). Positive zeta-potential dominance in most of the fractions can be explained because GBIB is a double positively charged molecule (scheme 1) while AOT bears a single negative charge. Also, CaS formation depends on the packing of the polar head group which changes after mixing GBIB:AOT in different solvent ratios [25].

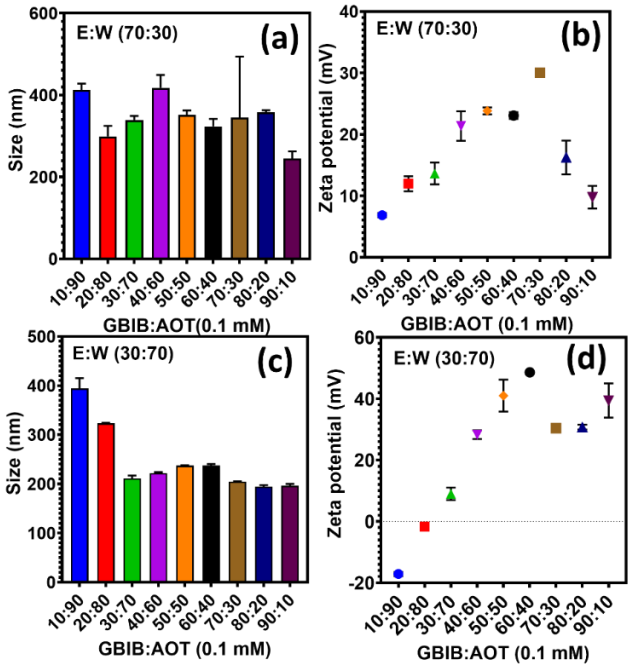

Fig. 3 Characterization of the synthesized GBIB:AOT fractions 0.1 mM concentration (a) hydrodynamic diameter and **(b)** zeta potential in E:W (70:30) mixture; GBIB:AOT fractions 0.1 mM **(c)** hydrodynamic diameter and **(d)** zeta potential in E:W (30:70) mixture.

3.2. Stability study: The stability of the formulated GBIB:AOT CaS was examined in E:W solvent mixture by measuring their hydrodynamic diameter for up to one month where in place of water we have used PBS (pH 7.4) to also study the effect of the salt on synthesized GBIB:AOT fractions in perspective to use it in cell media. Out of all these fractions, we have chosen one GBIB rich 80:20 and other AOT rich 20:80 fraction (0.1 mM) in three different solvent mixtures i.e. E:W (70:30), (50:50), and (30:70) solvent ratio. The calculated size and PDI values for GBIB:AOT fractions are given in Table 2 and intensity vs size (d, nm) graph was plotted (Fig. S2) which indicated the narrow size distribution of freshly prepared CaS. All the freshly prepared fractions have a size from 100 nm to 250 nm with very low PDI which also confirmed relatively narrow-size distribution of the particles. After two weeks, a growth in size was noted for the particles in E:W (70:30) solvent mixture, which after one month reached a size around 750 nm for both 20:80 and 80:20 fractions, along with a large increase

in PDI. In E:W (50:50) solvent ratio, a similar behaviour was observed in which size increase for both fractions with time, and after 1 month it reached ca. 568 nm and 987 nm for 20:80 and 80:20 fractions, respectively. However, in water-rich E:W (30:70) solvent mixture, for 20:80 fraction their size, remained nearly similar for up to 1 month, and for 80:20 fraction a slight surge in the size was noticed and reached up to ca. 388 nm. This revealed that CaS 20:80 and 80:20 fractions in water-rich E:W (30:70) solvent mixture has maximum stability without neither any sedimentation nor gelation for 1 month.

Table 2. DLS measured size and PDI values for stability study of the GBIB:AOT fractions in different E:W solvent ratios

E:W	GBIB:AOT	Fresh sample		After two weeks		After one month	
		Size* (nm)	PDI	Size* (nm)	PDI	Size* (nm)	PDI
70:30	20:80	240.6	0.10	528.9	0.86	713.7	0.78
	80:20	187.3	0.15	482	0.59	772.5	0.72
50:50	20:80	159.5	0.41	349.5	0.46	568.8	0.56
	80:20	143.5	0.23	243.7	0.45	987.5	0.56
30:70	**20:80**	**166.6**	**0.09**	**191**	**0.17**	**197.8**	**0.14**
	80:20	**174.3**	**0.21**	**226**	**0.31**	**387.9**	**0.65**

***given values of size and PDI are average of three measurements.**

3.3: Morphological study: FEG-SEM characterization was performed to further verify the CaS formation, as well as the morphological appearance of selected CaS (cationic rich 80:20 and anionic rich 20:80 GBIB:AOT) fractions in all E:W (70:30), (50:50) and (30:70) solvent ratios. All fractions images were captured, at scale bar 1 µm and their zoom-in image at 100 nm, as shown in Fig 4. In all the three solvent ratios, both cationic and anionic rich fractions exhibited the formation of spherical structures (Fig. 4(a)-(f)), and A population of small spherical CaS of size around 100 nm were observed. In 50:50 E:W solvent ratio (as given in Fig. 4(c)) along with spheres, some primordial fibres were also observed that were attached to the spherical structures. As we have reported previously, GBIB in E:W solvent ratio can form

long bilayer fibers, following a nucleation process and further conversion of particles to long fibres, which depend on temperature, concentration, and E:W solvent ratio [29,40].

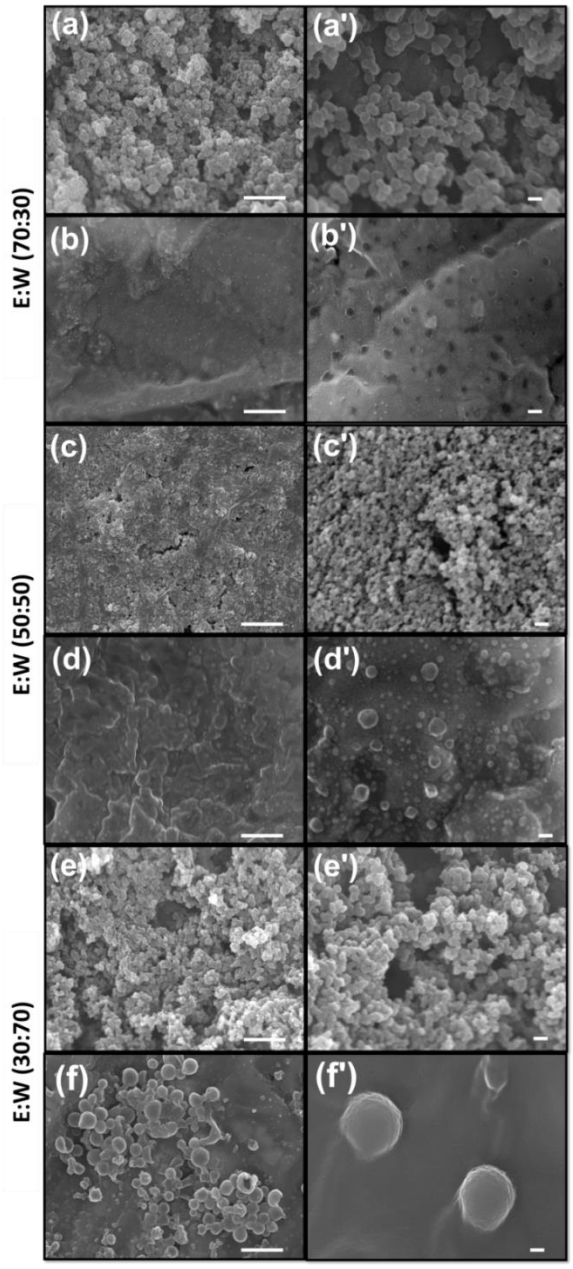

Fig. 4 Morphological characterization of the prepared CaS in different E:W solvent ratios. FEG-SEM images of GBIB:AOT fractions **(a)** 80:20 **(a')** zoom in image of 80:20, **(b)** 20:80 **(b')** zoom in image of 20:80, in E:W (70:30) solvent ratio. GBIB:AOT fractions **(c)** 80:20 **(c')** zoom in image of 80:20, **(d)** 20:80 **(d')** zoom in image of 20:80, in E:W (50:50) solvent

ratio. GBIB:AOT fractions **(e)** 80:20 **(e')** zoom in image of 80:20, **(f)** 20:80 **(f')** zoom in image of 20:80, in E:W (30:70) solvent ratio. Scale bar 1 µm and 100 nm (left and right), respectively.

3.4. PS encapsulation study: RB solution was prepared in E:W (70:30), (50:50) and (30:70) solvent ratios. Then RB containing CaS mixtures were prepared by following GBIB-RB-AOT mixing procedure. Fluorescence (Fig. S3(a-c)) and UV-visible absorption spectroscopy (Fig. S3(d-f)) were performed to validate the change in RB fluorescence emission intensity and absorbance with CaS and compared with free RB in respective E:W solvent ratio. In E:W (70:30) a decrease in the RB fluorescence intensity was observed in the presence of GBIB:AOT (80:20) fraction, as an indication of encapsulation. The decrease was higher in GBIB:AOT(80:20) fraction as compared to the (20:80) fraction at the same wavelength (Fig. S3((a)). Similar observations were made for the other two solvent ratios i.e. E:W (50:50) and (30:70) (as given in Fig. S3(b)&(c)). UV-visible absorption spectra in E:W (70:30) showed a decrease in absorption for both CaS (80:20) and (20:80) fractions with little bathochromic shift of around 5 nm in comparison to pure RB absorption maxima (Fig. S3(d)). However, in E:W (50:50) solvent ratio there was a large bathochromic shift (550 nm to 575 nm) with the decrease in absorption spectra of RB in presence of both 80:20 and 20:80 fractions (Fig. S3(e)). For RB with GBIB:AOT (20:80) in E:W (30:70) solvent ratio, there was more decrease in the absorption spectrum of RB with large bathochromic shift (555 nm to 583 nm) while for RB with (80:20) fraction the bathochromic shift from 555 nm to 564 nm was recorded (Fig. S3(f)). This strong bathochromic shift was the result of the strong electrostatic interaction between negatively charged RB and positively charged catansomes fractions.

Also, the variation in the zeta potential values of the above-formulated RB loaded CaS mixture was assessed in various E:W solvent ratios (Fig. S3(g)). In E:W (70:30) solvent ratio, both the GBIB:AOT fractions exhibited positive zeta-potential which confirmed that more dominance

of the GBIB towards the surface side. However in E:W (50:50), for RB loaded GBIB:AOT (20:80) fraction has –17 mV surface charge and 80:20 fraction had +20 mV. On the other hand, in E:W 30:70 solvent ratio, RB loaded 20:80 fraction has negative zeta potential value while 80:20 fraction have + 55 mV zeta potential (Fig. S3(g)). On comparing these obtained values with free CaS (Fig. 2&3), this is confirmed that on the addition of RB, both positive and negative charge containing RB@CaS were formed in E:W (50:50) and (30:70) solvent ratio.

Confocal microscopic analysis was used for RB containing GBIB:AOT (80:20) and (20:80) fractions in E:W (50:50) ratio (Fig. 5(a)&(b)). The images obtained illustrated that the 20:80 fraction showed spherical particles, and the confocal image and its gray value plot in Fig. 5(b)&(c) suggested that there is regular dissemination of RB on CaS. Similarly, for GBIB:AOT 80:20 fraction, DIC image showed (Fig. 5(d)) that small size CaS are attached to the long fibers. The confocal image (Fig. 5(e)), and its intensity profile graph (Fig. 5(f)), also confirmed that the RB containing catansomes are attached to fibers with uniform RB distribution on it.

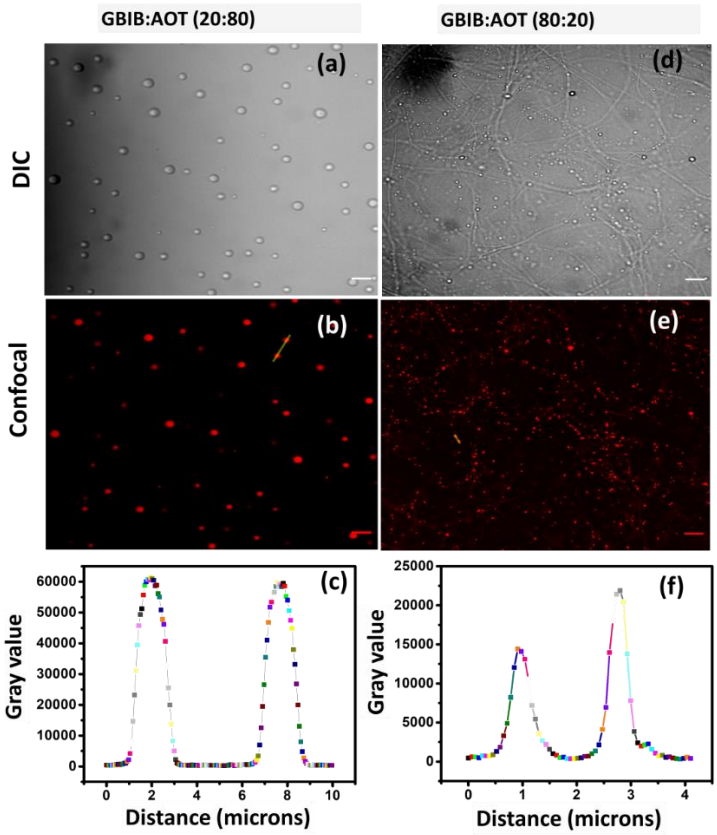

Fig. 5 Confocal laser scanning microscope measurements of RB encapsulation to catansomes in E:W(50:50). CLSM images of GBIB:AOT **(a)** DIC image (20:80), **(b)** confocal image of (20:80), **(c)** Gray value graph calculated from **(b),** and GBIB:AOT **(d)** DIC image (80:20), **(e)** confocal image of (80:20) and **(f)** Gray value graph calculated from **(e)** (scale bar is 5 μm).

3.5. Singlet oxygen generation study: Initially, the $^1O_2$ generation ability of the pure RB in different solvents like pure ethanol, E:W (70:30), (50:50), (30:70) solvent ratio and pure water was studied. A mixture of ABMA with RB was irradiated using a green diode laser (wavelength 532 nm, power 50 mW) in the above-mentioned three solvent ratios and pure solvents. There is a very minor diminution in the fluorescence intensity of free RB in pure ethanol (Fig. 6(a)). However, this decrease in the fluorescence intensity amplified as we increased the water content in E:W ratios from (70:30) to (50:50) to (30:70) to only water (Fig. 6(b),(c),(d), and (e)), respectively. This decline in ABMA fluorescence intensity was plotted vs time (Fig. 6(f)) which exhibited the clear sign that with the surge in the water content in the solvent mixture there is an increase in $^1O_2$ production by pure RB. The percentage rate of ABMA photobleaching was measured to compare the $^1O_2$ generation capability of RB. This rate was calculated for up to 60 sec at fixed RB (2 μM) concentration (Fig. 6(g)). It was 0.039% for pure RB in ethanol, 0.058% in E:W(70:30), 0.131% in E:W(50:50), 0.259% in E:W(30:70), and 0.484% in water. This confirmed that with an increase in water in the total E:W solvent ratios there was an increase in photobleaching of ABMA which represents more singlet oxygen generation. This can be rationalised because a PS's singlet oxygen generation capability depends on the local solvent medium used for PS solubilization. Singlet oxygen generation increase with more solubilization of PS and increases in excited triplet state quantum yield (ϕ_T). It is well reported that RB showed maximum solubility in water as compared to other solvents [41,42]. Gandin et al studied xanthene derivative ϕ_T and singlet oxygen quantum yield

in water and ethanol solvent. In water, RB has more intersystem crossing and ϕ_T in comparison to ethanol due to which RB has more singlet oxygen generated in water as compared to ethanol solvent [43,44].

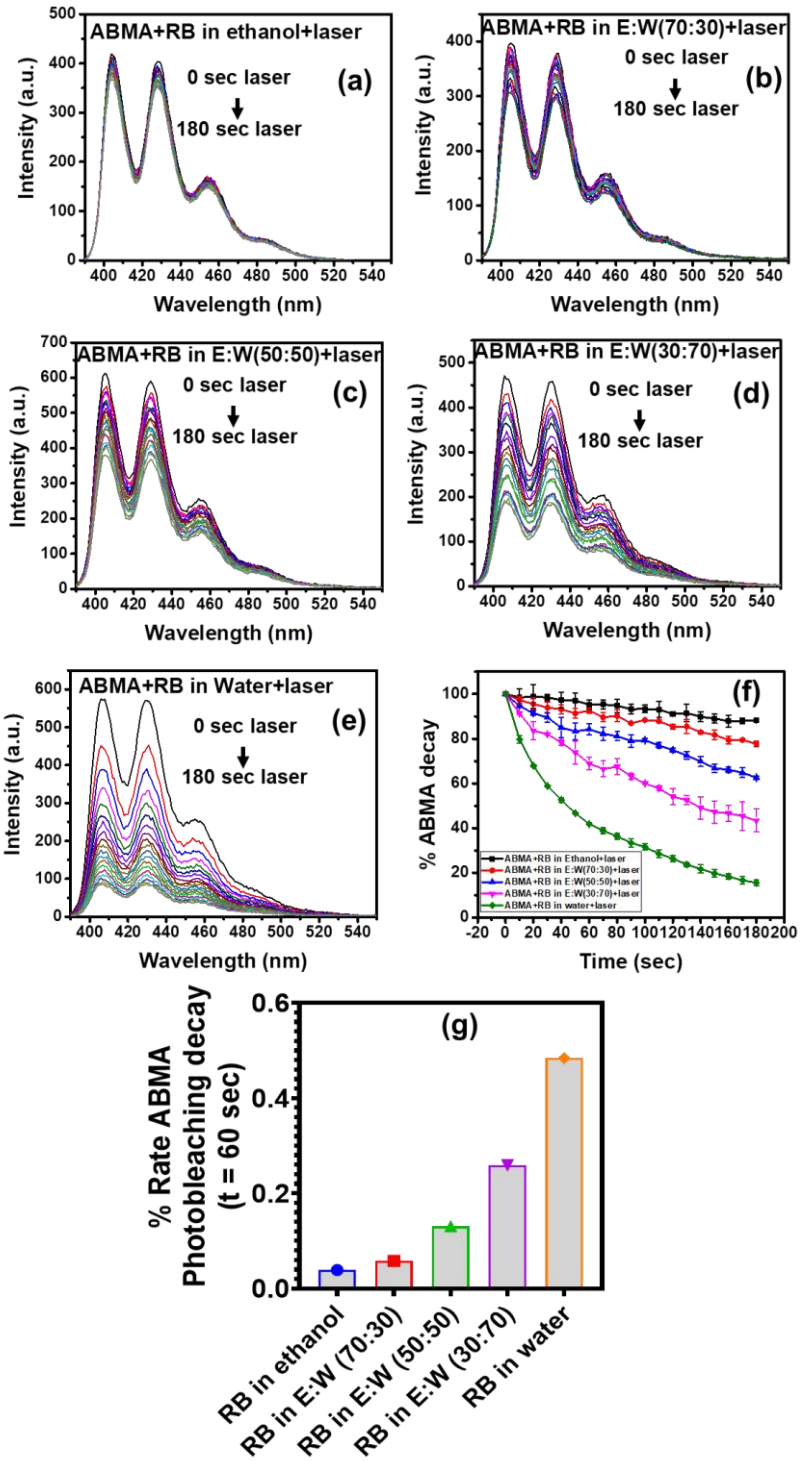

Fig. 6 Graph of the ABMA fluorescence intensity change after irradiation with different mixtures. Laser irradiation of RB and ABMA mixture dissolved in **(a)** ethanol, **(b)** E:W (70:30), **(c)** E:W (50:50), **(d)** E:W (30:70), **(e)** only water **(f)** percentage of ABMA decay calculated from all graph. **(g)** The percentage rate of ABMA photobleaching of RB solution in ethanol, in E:W (70:30), (50:50) and (30:70) and only water till 60 sec concerning RB concentrations. The averages and the error bars in (f) were determined from the three independent measurements.

Initially, the change in fluorescence intensity of ABMA was measured after laser irradiation on pure ABMA, ABMA with AOT, and ABMA with GBIB. There was no alteration in the fluorescence intensity of ABMA, which confirmed that there is no effect of laser light on the quencher, and also there was no singlet oxygen generation in presence of pure component GBIB and AOT when dissolved in their respective solvents (Fig. S4(a)-(c)). The $^1O_2$ generation with only RB (Fig. S5(a)) revealed decent diminution in ABMA fluorescence intensity (180-sec laser irradiation). Then, RB incorporated in different CaS fractions prepared in as studied E:W solvent ratios were explored for the $^1O_2$ generation study. Firstly, we tested the E:W (50:50), which showed a slight decrease in ABMA fluorescence intensity in the presence of GBIB:AOT (80:20) and (20:80) fractions (Fig. S5(b)&(c)). Upon mixing RB into these GBIB:AOT fractions, a remarkable decrease in the ABMA intensity was observed on irradiation with the laser light (Fig. S5(d)&(e)). The initial decrease in the intensity was more peculiar with RB@GBIB:AOT (80:20) fractions as compared to the RB@GBIB:AOT(20:80) fraction with RB. However, it became equal after 180-sec of laser irradiation. This large decrease in ABMA intensity confirms the vast surge in the $^1O_2$ generation upon the assimilation of RB into the GBIB:AOT catansome.

Further, the $^1O_2$ generation ability of RB@GBIB:AOT in E:W (30:70) and (70:30) solvent ratios were also studied. In the same experimental conditions, the solutions were prepared in

E:W (30:70) and (70:30) solvent ratio and then ABMA degradation under laser light irradiation was measured. As we have discussed earlier, more ABMA fluorescence intensity decrease was observed in water, therefore, more ABMA quenching was observed in water-rich E:W (30:70) solvent ratio with both GBIB:AOT (80:20) and (20:80) fractions (Fig. S6(a-d)). On the other hand, in E:W (70:30) solvent ratio, there is a very small decrease in ABMA quenching with pure RB and this quenching increases up to a small extent when RB was loaded into GBIB:AOT (80:20) and (20:80) fractions (Fig. S7(a-d). The calculated percentage of ABMA changes with time in different solvent ratios and is given in Fig. 7(a-c). For further comparison, the percentage rate of ABMA photobleaching was normalized using equation-1 after 60 sec for RB@GBIB:AOT in different E:W ratios and was compared with pure RB. This calculated photobleaching rate is given in Fig. 7(d).The obtained value in E:W (70:30) for free RB was 0.058% while RB with GBIB:AOT (80:20) and (20:80) was 0.098% and 0.133%, respectively. Similarly, value for RB in E:W(50:50) was 0.18% and it increases to 0.79% and 0.71% with 80:20 and 20:80 fractions, respectively. This also elucidates a large increase in the singlet oxygen efficiency of RB@CaS in E:W(50:50). In E:W (30:70) the value for free RB was 0.22% and it increase to 0.70% and 0.62% with GBIB:AOT (80:20) and (20:80) fraction, respectively. Overall these results confirmed that RB $^1O_2$ production efficiency increase in presence of catansomes mixtures and also upsurges with an increase in the water content in E:W solvent ratio. Additionally, in most of the cases after incorporating RB into CaS a rise in singlet oxygen generation efficiency was prominent in the presence of GBIB rich fraction i.e. 80:20 fraction as compared to AOT rich fraction 20:80. It was reported that cationic GBIB in nanofiber gelation form also helped in promoting singlet oxygen efficiency of tetra anionic 5,10,15,20-tetrakis(4-carcoxylatephenyl)porphyrin [40]. In this case, GBIB based catansome is helping in promoting $^1O_2$ generation ability of RB to a larger extent.

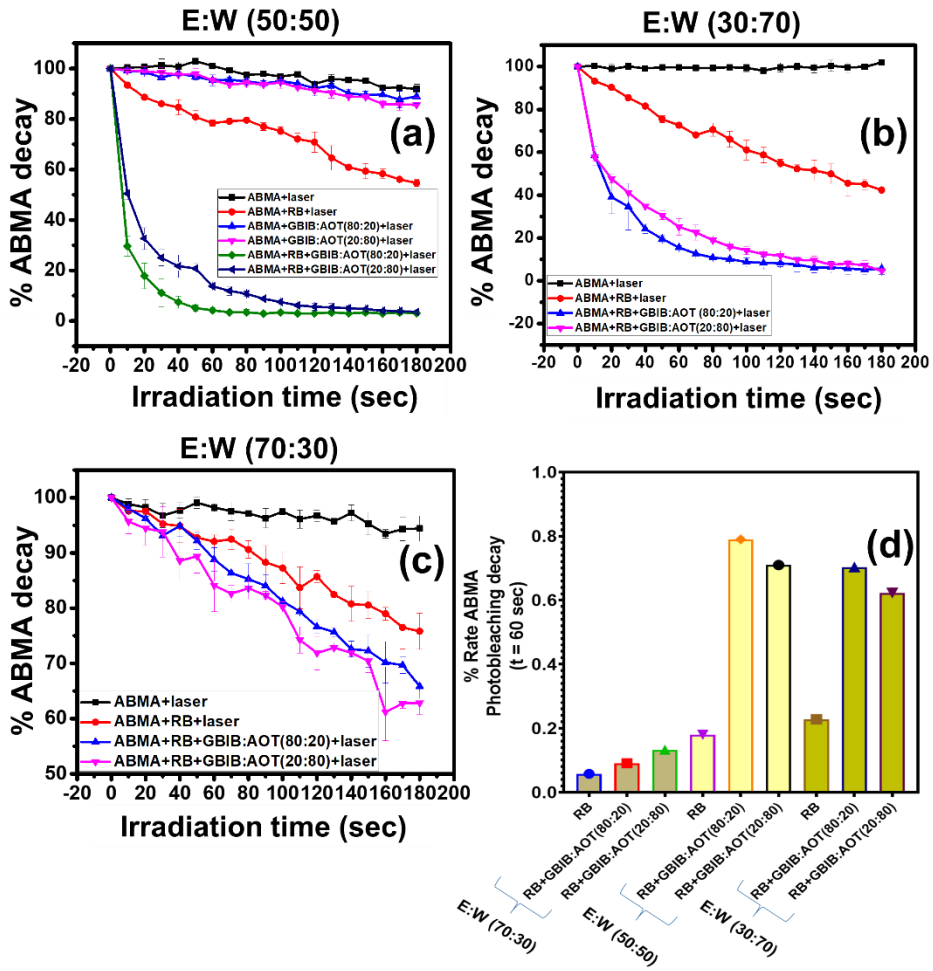

Fig. 7 Graph of the ABMA fluorescence intensity decay in presence of RB-loaded CaS. % ABMA fluorescence emission decay with RB loaded GBIB:AOT (80:20) and (20:80) fractions in **(a)** E:W (50:50), **(b)** E:W (30:70) and **(c)** E:W (70:30) solvent ratios, **(e)** The percentage rate of ABMA photobleaching with RB loaded GBIB:AOT (80:20) and (20:80) fractions in E:W (70:30), (50:50) and (30:70) till 60 sec concerning RB concentrations. The averages and the error bars in (f) were determined from the three independent measurements.

3.6. Evaluation of dark toxicity, phototoxicity, and cellular uptake study: The cytotoxicity of different solvents is well known; for instance, Nguyen et al. have reported that pure ethanol is tolerable up to 1.25 % by MCF-7 cancer cell lines [45]. To reduce the cytotoxic effect of ethanol, in the present study we also applied 0.1 % of ethanol in various E:W solvent ratios for

in vitro study. As a result, only the water-rich E:W (30:70) fraction was chosen for the cellular study. WST-8 assay, which is very sensitive to provide information about the metabolic report of MCF-7 cells, was employed to verify the sublethal impact. Initially, the dark toxicity was evaluated by incubating pure RB (2 µM), only CaS, and RB@CaS (80:20) and RB@CaS (20:80) fractions at 1, 2, 5, 7.5, and 10 µM total concentration of surfactants in the CaS. There was no significant change in the cell metabolic activity in the dark condition indicating the biocompatibility of RB, CaS 80:20 and 20:80 fractions and RB@CaS(80:20) and RB@CaS(20:80) fractions (Fig. 8(a)). Next, out of these five CaS concentrations, only two concentrations (5 and 10 µM) of CaS were selected with RB to determine the phototoxicity. There was no significant effect of neither the green laser light (control) nor the CaS without RB on the MCF-7 cell % metabolic activity (Fig. 8(b)). However, there was a significant concentration-dependent diminution in metabolic activity upon illuminating with RB-loaded CaS. Specifically, irradiation with RB@CaS (80:20) fraction at 5 and 10 µM caused a 50% and 85% reduction in metabolic activity, respectively. On the other hand, with RB-loaded CaS (20:80) fraction of CaS at 5 and 10µM concentration caused 40% and 50% reduction in metabolic activity, respectively (Fig. 8(b)). This experiment showed that GBIB rich fraction i.e. 80:20 encapsulating RB exhibited excellent phototoxicity as compared to AOT rich 20:80 fraction. The fact that neither pure RB nor CaS did not prompt any change in the metabolic activity, signifyies the role of CaS with RB-loaded CaS which improved the phototoxicity of RB.

To investigate whether the distinctive exposure to RB-loaded CaS was due to variations in their uptake, we evaluated the MCF-7 cells' intracellular uptake of RB using a fluorescence microscope (Fig. 8(c-f)). MCF-7 cells were incubated for 48 h with free RB, RB-loaded (80:20) and (20:80) CaS (10 µM) and counterstained with DAPI (blue) to assess the appropriate localization of RB fluorescence. MCF-7 cells showed strong fluorescence with RB-loaded

CaS, however, weak fluorescence intensity was observed with free RB. The cationic rich GBIB:AOT (80:20) fraction acted as an excellent transporting agent. The fraction with more GBIB-rich side i.e. 80:20 showed superior RB uptake as compared to 20:80 fraction (Fig. 9(d&e)). Less uptake of free RB could be because RB has a negative charge which matches with a surface charge of MCF-7 cells (ζ = -20 mV) [46] which obstructs its uptake. However, positive charge containing RB-loaded CaS caused a strong electrostatic interaction which enhanced its uptake into the MCF-7 cells. This divergent cellular uptake profile of RB explicates the attained variation in the phototoxicity of free RB and RB-loaded CaS (80:20 & 20:80) fractions. Thus, this experiment verified that the formulated GBIB:AOT CaS fractions are biocompatible for RB PS delivery, which due to their catanionic nature enhanced the cellular uptake.

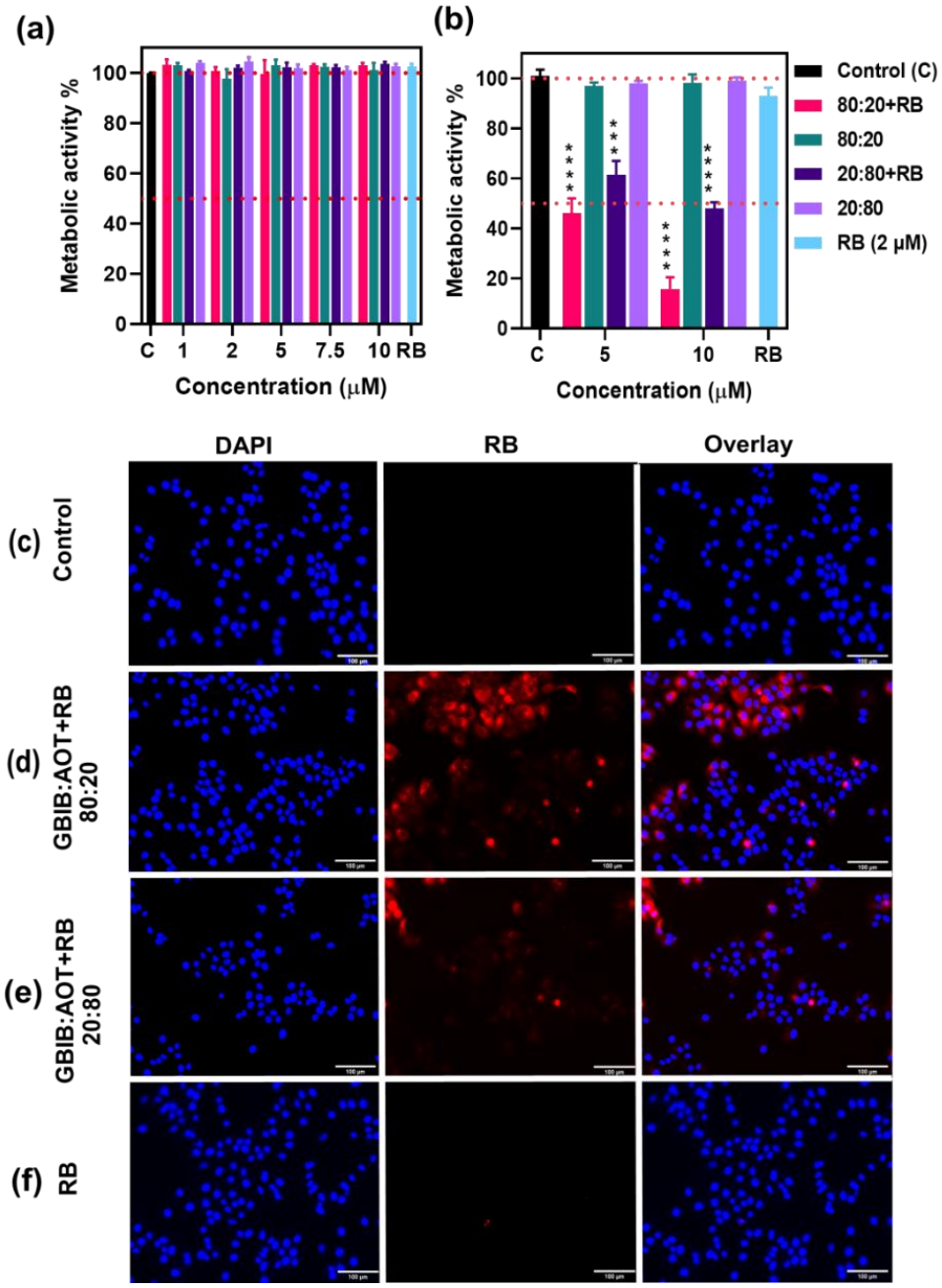

Fig. 8 RB-loaded CaS cytotoxicity and uptake study on MCF-7 cells. Graph of MCF-7 cells metabolic activity **(a)** Dark-toxicity and **(b)** phototoxic study of RB, CaS and RB-loaded CaS at different concentrations were assessed by utilizing WST-8 assay. The experiment was done employing triplicates and the data are articulated as mean ± S.E.M. Statistical significance at ****$p < 0.0001$ *vs* untreated control (denoted as C) was calculated using 2-way ANOVA with Tukey post-test. **(c-f)** MCF-7 cellular uptake of RB-loaded CaS analysed by using a fluorescence microscope at 20x. DAPI (Blue) – Nucleus. Scale bars = 100 μm

3.7. Intracellular $^1O_2$ generation study of RB loaded CaS: After confirming the phototoxicity ability of the RB loaded CaS, SOSG assay, which explores the mechanistic studies to confirm the intracellular $^1O_2$ generation, was performed [47,48]. MCF-7 cells were incubated with RB-loaded CaS (80:20) and (20:80) fraction (5 or 10 µM) and then irradiated with a green diode laser (wavelength 532 nm and power 50 mW) for 5 min. These cells were analyzed in the fluorescence microscope immediately after irradiation to show intense concentration-dependent green fluorescence (Fig. 9) with RB loaded (80:20) CaS as compared to (20:80) fraction. However, only RB and untreated cells showed weak fluorescence or no fluorescence, respectively. This experiment confirmed that RB-loaded CaS promote excessive intracellular $^1O_2$ generation and which correspondingly showed a higher phototoxicity effect toward MCF-7 cells.

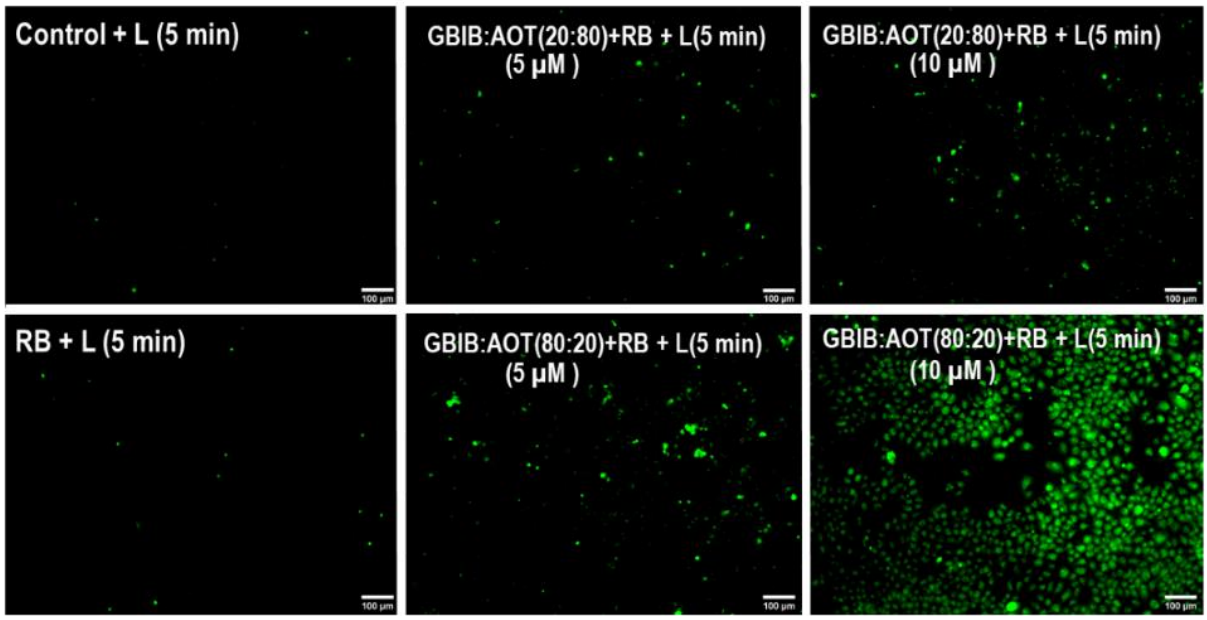

Fig. 9 MCF-7 cells intracellular $^1O_2$ detection study by SOSG assay after applying PDT dose of RB-loaded catansomes (scale bar 100 µm).

4. Conclusion: We have described the preparation of catansomes (CaS) self-assembled from a mixture of a gemini imidazolium-based (GBIB) surfactant and an anionic AOT surfactant in different ethanol:water (E:W) solvent ratios, i.e. (70:30), (50:50) and (30:70). An easy and inexpensive solution-solution mixing method was employed which spontaneously formed catansomes with variation in size and zeta-potential at different concentrations (1 mM and 0.1 mM). DLS confirmed that CaS at low concentration (0.1 mM) in all studied E:W solvent ratios have diameters from 200 to 300 nm and their size increased with the increase in the total concentration of GBIB:AOT mixture which later shows gelation after 3 to 4 days. The prepared CaS possess long-term stability for up to one month in E:W (30:70) solvent ratio, and FEG-SEM confirms their spherical morphology. RB loading into CaS was confirmed by confocal laser microscope, fluorescence, and UV-visible absorption spectroscopies. The prepared GBIB:AOT, specially GBIB rich fractions in E:W (50:50) and (30:70) solvent ratio further enhanced the ABMA photobleaching rate. These CaS signify a vital role of gemini surfactant in the enhancement of the single oxygen generation ability of RB. Finally, phototoxicity of RB-incorporated CaS in E:W (30:70) system was investigated *in-vitro* on MCF-7 human breast cancer cells. These catansomes depict high biocompatibility with no dark toxicity effect. After irradiation for 5 min in the presence of RB loaded GBIB:AOT (80:20) fraction resulted in 90% drastic decrease in metabolic activity of MCF-7 cells. SOSG assay confirmed the concentration-dependent intracellular $^1O_2$ generation in MCF-7 cells. This experiment confirmed the increase in $^1O_2$ generation of RB with an increase in water content in the E:W solvent ratio and a further increase was observed when incorporated photosensitizer was incorporated into catansomes which efficiently decreased the cell metabolic activity. The RB uptake facilitation and enhancement in $^1O_2$ generation by GBIB rich CaS makes the nanomaterial a strong candidate for photosensitizer´s delivery vehicle which will find further use in photomedicine.

ORCID ID:

Bunty Sharma: 0000-0003-2495-6288

Mario Samperi: 0000-0003-4362-2574

Akhil Jain: 0000-0003-2019-2030

Ganga Ram Chaudhary: 0000-0003-0501-6071

Gurpreet Kaur: 0000-0002-8985-3186

Lluïsa Pérez-García: 0000-0003-2031-4405

Author Contributions:

Bunty Sharma: Conceptualization, Formal analysis, Investigation, Methodology, Original draft preparation, **Mario Samperi*:** Conceptualization, Methodology, Investigation, Original draft preparation, **Akhil Jain*:** Conceptualization, Methodology, Validation, Investigation, Formal analysis, Original draft preparation, **Ganga Ram Chaudhary:** Supervision, Funding, **Gurpreet Kaur:** Conceptualization, Supervision, Funding, Visualization, Writing Reviewing, and Editing, **Lluïsa Pérez-García:** Conceptualization, Supervision, Resources, Funding, Validation, Visualization, Original draft preparation, Writing Reviewing, and Editing

*** These two co-autors contributed equally to the work**

Conflicts of Interest: The authors declare no conflict of interest.

Acknowledgments: B. S. thanks the Commonwealth split-site scholarship (INCN-2019-409) and DST INSPIRE SRF (IF170098). This work was supported by project PID2020-115663GB-C32 funded by MCIN/ AEI /10.13039/501100011033. Authors are thankful to F. J. Rawson for providing financial support by the Engineering and Physical Sciences Research Council project [grant numbers EP/R004072/1, EP/L022494/1]. The authors also thank Vincent K. K. Tang and Nicole Hoi-Ching Woo for preliminary experiments, the NMRC and School of Life Sciences Imaging (SLIM) at the University of Nottingham for the instrumentation and facility provided.

References:

[1]. D. E. J. G. Dolmans, D. Fukumura and R. K. Jain, Photodynamic therapy for cancer, *Nat. Rev. Cancer*, 3(2003), 380-387.

[2]. P. R. Ogilby, Singlet oxygen: there is indeed something new under the sun, *Chem. Soc. Rev*., 39(2010), 3181-3209.

[3]. M. A. Filatov and M. O. Senge, Molecular devices based on reversible singlet oxygen binding in optical and photomedical applications, *Mol. Syst. Dex. Eng*., 1(2016), 258-272.

[4]. J. P. Celli, B. Q. Spring, I. Rizvi, C. L. Evans, K. S. Samkoe, S. Verma, B. W. Porque and T. Hasan, Imaging and photodynamic therapy mechanisms, monitoring, and optimization, *Chem. Rev*., 110(2010), 5, 2795-2838.

[5]. H. Sun, M. Feng, S. Chen, R. Wang, Y. Luo, B. Yin, J. Li and X. Wang, Near-infrared photothermal liposomal nanoantagonists for amplified cancer photodynamic therapy, *J. Mater. Chem. B*, 8(2020), 7149-7159.

[6]. S. Callaghan and M. O. Senge, The good, the bad, and the ugly-controlling singlet oxygen through design of photosensitizers and delivery systems for photodynamic therapy, *Photochem. Photobiol. Sci*., 17(2018), 1490-1514.

[7]. A. Jain, R. Koyani, C. Muñoz, P. Sengar, O. E. Contreras, P. Juárez and G. A. Hirata, Magnetic-luminescent cerium-doped gadolinium aluminium garget nanoparticles for simultaneous imaging and photodynamic therapy of cancer cells, *J. Colloid Interface Sci*., 526(2018), 220-229.

[8]. B. Sharma, G. Kaur, G. R. Chaudhary, Optimization and utilization of single chain metallocatanionic vesicles for antibacterial photodynamic therapy against E. coli, *J. Mater. Chem. B*, 8(2020), 9304-9313.

[9]. R. F. Donnelly, P. A. M. Carron and M. M. Tunney, Antifungal photodynamic therapy, *Microbiol. Res*., 163(2008), 1-12.

[10]. C. Wang, L. Cheng and Z. Liu, Upconversion nanoparticles for photodynamic therapy and other cancer therapeutics, *Theranostics*, 3(2013), 317-330.

[11]. N. Kipshidze, N. Yeo and N. Kipshidze, Photodynamic therapy for COVID-19, *Nature Photonics*, 14(2020), 651-652

[12]. V. A. Svyatchenko, S. D. Nikonova, A. P. Mayorov, M. L. Gelfond, V. B. Loktev, Antiviral photodynamic therapy: inactivation and inhibition of SARS-CoV-2 in vitro using methylene blue and Radachlorin, *Photodiagnosis Photodyn. Ther.*, 33(2021), 102112.

[13]. J. Arnbjerg, M. Johnsen, C. B. Nielsen, M. Jorgensen and P. R. Ogilby, Effect of sensitizer protonation on singlet oxygen production in aqueous and nonaqueous media, *J. Phys. Chem. A*, 111(2007), 4573-4583.

[14]. S. Ben-Dror, I. Bronshtein, A. Wiehe, B. Order, M. O. Senge and B. Ehrenberg, On the correlation between hydrophobicity, liposome binding and cellular uptake of porphyrin sensitizers, *Photochem. Photobiol*, 82(2006), 695-701.

[15]. W. Spiller, H. Kliesch, D. Wohrle, S. Hackbarth, B. Order and G. Schnurpfeil, Singlet oxygen quantum yields of different photosensitizers in polar solvents and micellar solution, *J. Porphyrins Phthalocyanines*, 2(1998), 145-158.

[16]. M. Kuruppuarachchi, H. Savoie, A. Lowry, C. Alonso and R. W. Boyle, Polyacrylamide nanoparticles as a delivery system in photodynamic therapy, *Mol. Pharmaceutics*, 8(2011), 920-931.

[17]. R. Zagami, G. Sortino, E. Caruso, M. C. Malacarne, S. Banfi, S. Patane, L. Monsu-Scolaro, and a. Mazzaglia, Tailored-BODIPY/amphiphiic cyclodextrin nanoassemblies with PDT effectiveness, *Langmuir*, 34(2018), 8639-8651.

[18]. Q. Chen, M. Yanhong, J. Zhao, Z. Mei, L. Wenjing, Q Liu, L. Xiong, W. Wu and Z. Hing, In vitro and in vivo evaluation of improved EGFR targeting peptide-conjugated phthalocyanine photosensitizers for tumor photodynamic therapy, *Chin. Chem. Lett*., 29(2018), 171-1178.

[19]. G. A. de Souza, F. C. Bezerra and T. D. Martins, Photophysical properties of fluorescent self-assembled peptide nanostructures for singlet oxygen generation, *ACS Omega*, 5(2020), 8804-8815.

[20]. D. Kessel, A. Morgan and G. M. Garbo, Sites and efficacy of photodamage by tin etiopurpurin in vitro using different delivery systems, *Photochem. Photobiol*., 54(1991), 193-196.

[21]. K. C. Wu, Z. L. Huang, Y. M. Yang, C. H. Chang and T. H. Chou, Enhancement of catansomes formation means of cosolvent effect: Semi-spontaneous preparation method, *Colloids Surf. A Physicochem. Eng. Asp*, 302(2007), 599-607.

[22]. K. R. Rosholm, A. Arouri, P. L. Hansen, A. G. Perez and O. G. Mouritsen, Characterization of fluorinated catansomes: A promising vector in drug-delivery, *Langmuir*, 28(2012), 2773-2781.

[23]. P. Verma and K. Pathak, Therapeutic and cosmeceutical potential of ethosomes: an overview, *J. Adv. Pharm. Technol. Res*., 1(2010), 274-282.

[24]. E. W. Kaler, A. K. Murthy, B. E. Rodriguez and J. A. Zasadzinski, Spontaneous vesicles formation in aqueous mixtures of single-tailed surfactants, *Science*, 245(1989), 1371-1374.

[25]. B. Sharma, G. Kaur, G. R. Chaudhary, S. L. Gawali and P. A. Hassan, High antimicrobial photodynamic activity of photosensitizer encapsulated dual-functional metallocatanionic vesicles against drug-resistant bacteria S. aureus, *Biomater. Sci.*, 8(2020), 2905-2920

[26]. B. Sharma, V. Thakur, G. Kaur and G. R. Chaudhary, Efficient photodynamic therapy against Gram-positive and Gram-negative bacteria using Rose Bengal encapsulated metallocatanionic vesicles in presence of visible light, *ACS Appl. Bio Mater*., 3(2020), 8515-8524.

[27]. N. Sarma, J. M. Borah, S. Mahiuddin, H. A. R. Gazi, B. Guchhait and R. Biswas, Influence of chain length of alcohols on stokes' shift dynamics in catanionic vesicles, *J. Phy. Chem. B*, 115(2011), 9040-9049.

[28]. S. J. Yeh, Y. M. Yang and C. H. Chang, Cosolvent effects on the stability of catanionic vesicles formed from ion-pair amphiphiles, *Langmuir*, 21(2005), 6179-6184.

[29]. M. Samperi, L. Pérez-García and D. B. Amabilino, Quantification of energy of activation to supramolecular nanofibre formation reveals enthalpic and entropic effects and morphological consequence, *Chem. Sci*., 10(2019), 10256-10266.

[30]. M. Samperi, B. Bdiri, C. D. Sleet, R. Markus, A. R. Mallia, L. Pérez-García and D. B. Amabilino, Light-controlled micron-scale molecular motion, *Nat. Chem*., https://doi.org/10.1038/s41557-021-00791-2.

[31]. L. Casal-Dujat, M. Rodrigues, A. Yagüe, A. C. Calpena, D. B. Amabilino, J. G. Linares, M. Borràs and L. Pérez-García, Gemini imidazolium amphiphiles for the synthesis, stabilization, and drug delivery from gold nanoparticles, *Langmuir*, 28(2012), 2368-2381.

[32]. R. C. F. G. Lopes, O. F. Silvestre, A. R. Faria, M. L. C. do Vale, E. F. Marques and J. B. Nieder, Surface charge tunable catanionic vesicles based on serine-derived surfactants an efficient nanocarriers for the delivery of the anticancer drug doxorubicin, *Nanoscale*, 11(2019), 5932-5941.

[33]. M. E. Alea-Reyes, O. Penon, P. Garcia Calavia, M. J. Marín, D. A. Russell, L. Pérez-García, Synthesis and in vitro phototoxicity of multifunctional Zn (II)mesotetrakis(4-

carboxyphenyl) porphyrin-coated gold nanoparticles assembled via axial coordination with imidazole ligands, *J. Colloid Interface Sci*., 521(2018), 81-90.

[34]. T. Entradas, S. Waldron and M. Volk, The detection sensitivity of commonly used singlet oxygen probes in aqueous environments, *J. Photochem. Photobiol. B, Biol*., 204(2020), 111787.

[35]. X. Q. Zhou, M. Xiao, V. Ramu, J. Hilgendorf, X. Li, P. Papadopoulou, M. A. Siegler, A. Kros, W. Sun and S. Bonnet, The self-assembly of a cyclometalated palladium photosensitzer into protein-stabilized nanorods triggers, *J. Am. Chem. Soc*., 142(2020), 10383-10399.

[36]. O. Penon, M. J. Marín, D. A. Russell and L. Pérez-García, Water soluble, multifunctional antibody-porphyrin gold nanoparticles for targeted photodynamic therapy, *J. Colloid Interface Sci*., 496(2017), 100-110.

[37]. H. Chen, J. Tian, W. He and Z. Guo, H_2O_2-activatable and O_2-evolving nanoparticles for highly efficient and selective photodynamic therapy against hypoxic tumor cells, *J. Am. Chem. Soc*., 137(2015), 1539-1547.

[38]. W. Sun, L. Luo, Y. Feng, Y. Qiu, C. Shi, S. Meng, X. Chen and H. Chen, Gadolinium-rose bengal coordination polymer nanodots for MR-/fluorescence-image-guided radiation and photodynamic therapy, *Adv. Mater*., 32(2020), 2000377.

[39]. Y. Liu, C. F. Wen and Y. M. Yang, Development of ethosome-like catanionic vesicles for dermal drug delivery, *J. Taiwan Inst. Chem. E*., 43(2012), 830-838.

[40]. M. Samperi, D. Limón, D. B. Amabilino and L. Pérez-García, Enhancing singlet oxygen generation by self-assembly of a porphyrin entrapped in supramolecular fibres, *Cell Rep*., 1(2020), 100030.

[41]. M. C. De Rosa and R. J. Crutchley, Photosensitized singlet oxygen and its applications, *Coord. Chem. Rev*., 233(2002), 351-371.

[42]. A. Sivery, F. Anquez, C. Pierlot, J. M. Aubry and E. Courtade, Singlet oxygen ($^1O_2$) generation upon 1270 nm laser irradiation of ground state oxygen ($^3O_2$) dissolved in organic solvents: Simultaneous and independent determination of $^1O_2$ production rate and reactivity with chemical traps, *Chem. Phys. Lett*., 555(2013), 252-257.

[43]. E. Gandin, Y. Lion and A. V. De Vors, Quantum yield of singlet oxygen production by xanthene derivatives, *Photochem. Photobiol*., 37(1983), 271-278.

[44]. T. Entradas, S. Waldron and M. Volk, The detection sensitivity of commonly used singlet oxygen probes in aqueous environments, *J. Photochem. Photobiol. B. Biol*., 204(2020), 111787.

[45]. S. T. Nguyen, H. T. L. Nguyen and K. D. Truong, Comparative cytotoxic effects of methanol, ethanol and DMSO on human cancer cell lines, *Biomed. Res. Ther*., 7(2020), 3855-3859.

[46]. Y. Zhang, M. Yang, J. H. Park, J. Singelyn, H. Ma, M. J. Sailor, E. Ruoslahti, M. Ozkan and C. Ozkan, A surface-charge study on cellular-uptake behavior of F3-peptide-conjugated iron oxide nanoparticles, *Small*, 5(2009), 1990-1996.

[47]. Z. L. Yang, W. Tian, Q. Wang, Y. Zhao, Y. L. Zhang, Y. Tian, Y. X. Tang, S. J. Wang, Y. Liu, Q. Q. Ni, G. M. Lu, Z. G. Teng and L. J. Zhang, Oxygen-evolving mesoporous organosilica coated prussian blue nanoplatform for highly efficient photodynamic therapy of tumors, *Adv. Sci*., 5(2018), 1700847.

[48]. X. Ragas, A. J. Banzo, D. S. Garcia, X. Batllori and S. Nonell, Singlet oxygen photosensitisation by the fluorescent probe singlet oxygen sensor green, *Chem. Commun*., (2009), 2920-2922.

Supplementary material

Gemini surfactant mediated catansomes for enhanced singlet oxygen generation of Rose Bengal and their phototoxicity against cancer cells

Bunty Sharma[a,b], Mario Samperi[b,1], Akhil Jain[c], Ganga Ram Chaudhary[a], Gurpreet Kaur[a*] and Lluïsa Pérez-García[b,d,e*]

[a] Department of Chemistry, Centre for Advanced Studies in Chemistry, Panjab University, Chandigarh-160014, India

[b] Division of Advanced Materials and Healthcare Technologies, School of Pharmacy, University of Nottingham, Nottingham NG7 2RD, UK

[c] Division of Regenerative Medicine and Cellular Therapies, School of Pharmacy, University of Nottingham, Nottingham NG7 2RD, UK

[d] Departament de Farmacologia, Toxicologia i Química Terapèutica, Facultat de Farmàcia i Ciències de l'Alimentació, Avda. Joan XXIII 27-31, Universitat de Barcelona, 08028 Barcelona, Spain

[e] Institut de Nanociència i Nanotecnologia UB (IN2UB), Universitat de Barcelona, 08028 Barcelona, Spain

*corresponding authors: Lluïsa Pérez-García (email: mlperez@ub.edu)

Gurpreet Kaur (e-mail: gurpreet14@pu.ac.in)

[1] Present address: Istituto di Tecnologie Avanzate per l'Energia "Nicola Giordano" - CNR-ITAE, Messina, Italy

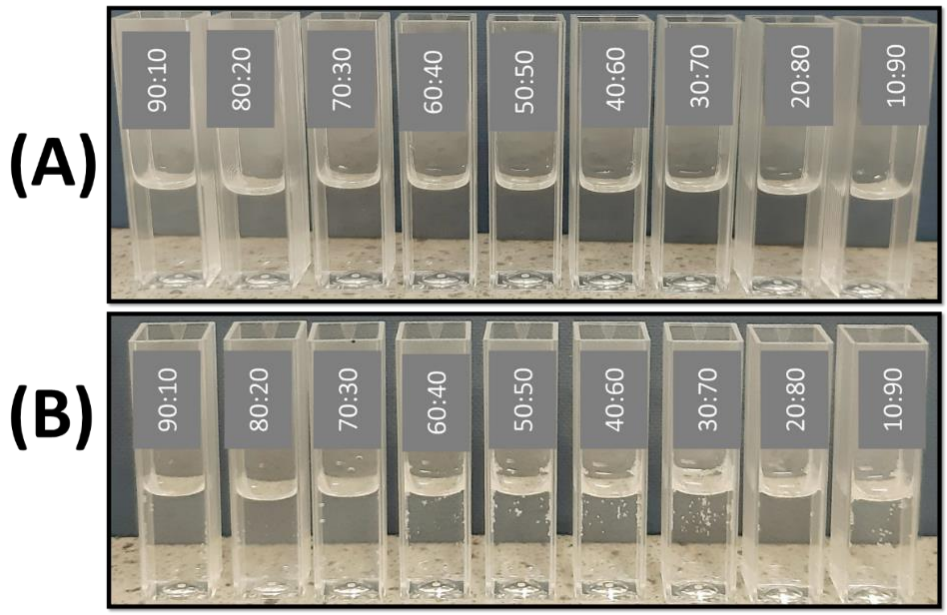

Fig. S1 Picture of the assembled GBIB:AOT (0.1 mM) fractions in (A) E:W (70:30) mixture and (B) in E:W (30:70) mixture.

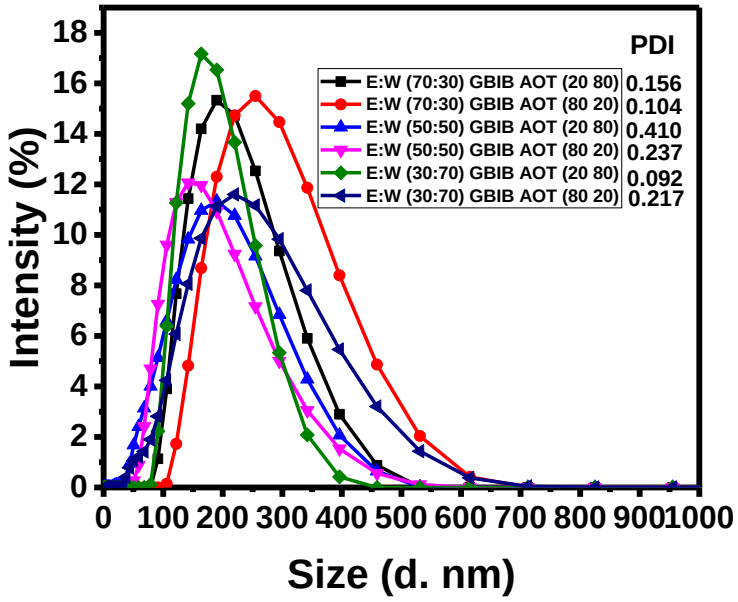

Fig. S2 Size vs intensity plot of GBIB:AOT mixture in E:W (PBS)

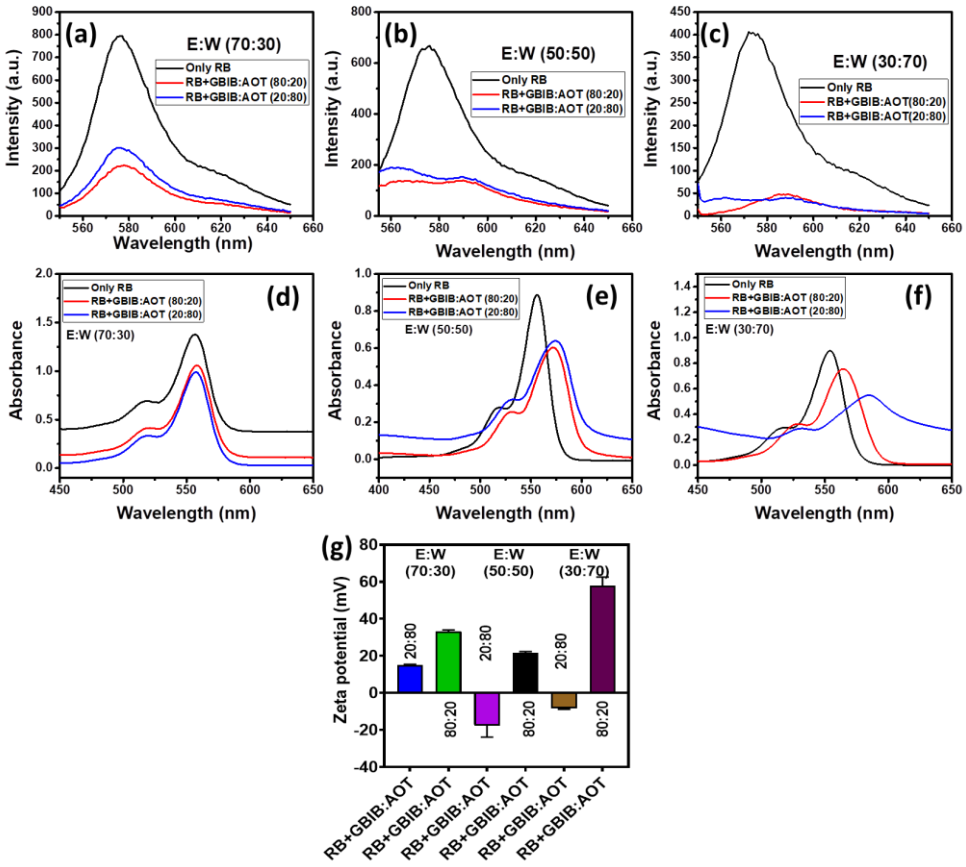

Fig. S3 F**luorescence intensity and UV-visible absorption spectroscopy study of RB with catansomes.** Fluorescence emission spectra of only RB, RB with GBIB:AOT (80:20) and (20:80) fraction in **(a)** E:W (70:30), **(b)** E:W (50:50), and **(c)** E:W (30:70) solvent ratios. UV-visible absorption spectra of only RB, RB with GBIB:AOT (80:20) and (20:80) fraction in **(d)** E:W (70:30), **(e)** E:W (50:50) and **(f)** E:W (30:70) solvent ratios. **(g)**Graph of the GBIB:AOT zeta potential change with RB in different E:W solvent ratios. The averages and the error bars in (g) were determined from the three independent measurements.

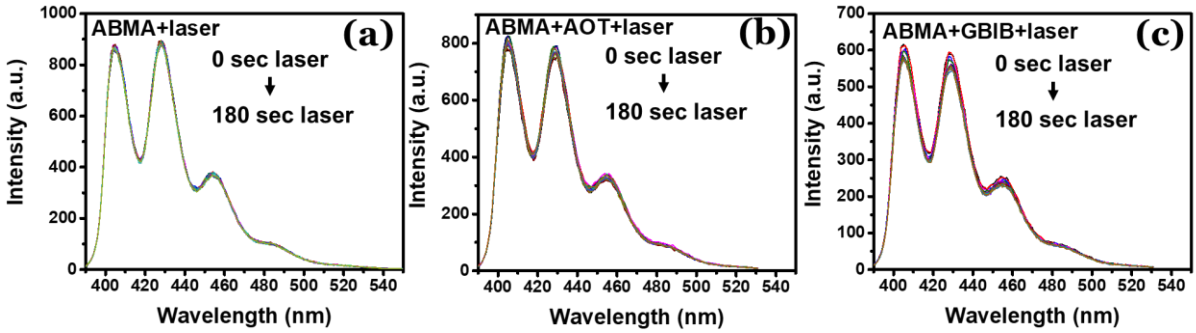

Fig. S4 ABMA fluorescence intensity decay with laser light (a) in ethanol (b) with AOT in water (c) with GBIB in ethanol.

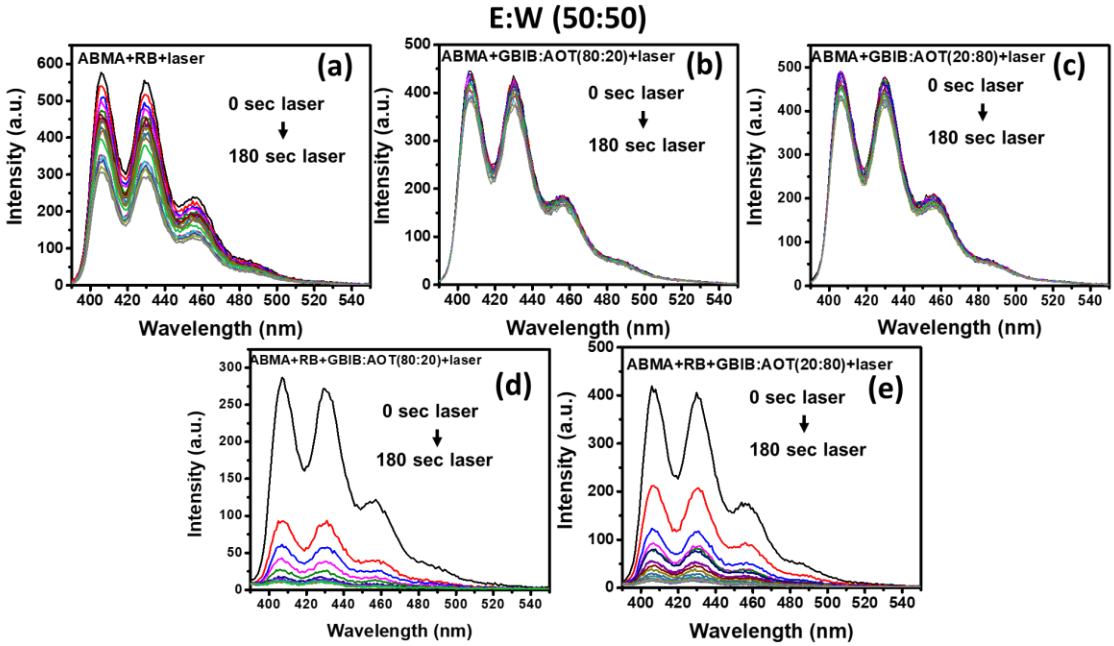

Fig. S5 ABMA fluorescence intensity change in E:W (50:50) solvent after laser irradiation. Laser illumination on ABMA mixture with **(a)** RB, **(b)** GBIB:AOT(80:20), **(c)** GBIB:AOT(20:80), **(d)** RB+GBIB:AOT(80:20), **(e)** RB+GBIB:AOT(20:80).

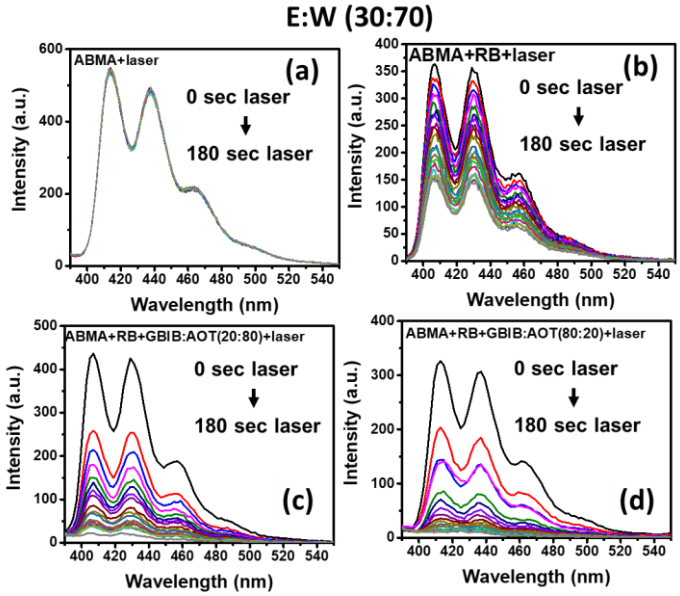

Fig. S6 ABMA fluorescence intensity decay upon irradiation (Wavelength 532 nm and power 50 mW) in E:W (30:70) in (a) only, as control (b) RB (c) RB + GBIB:AOT (20:80) and (d) RB + GBIB:AOT(80:20).

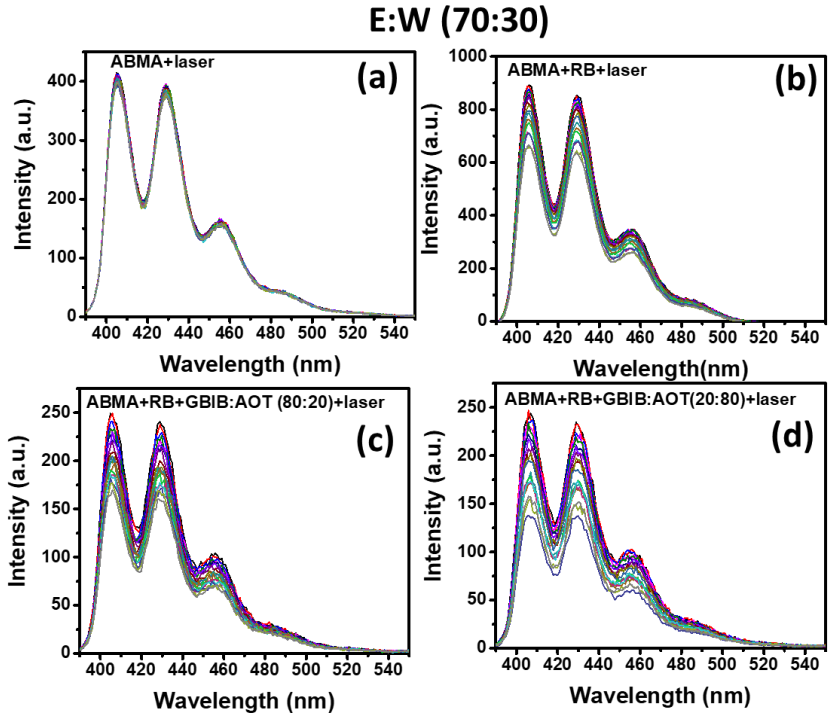

Fig. S7 ABMA fluorescence intensity decay upon irradiation in E:W (70:30) with (a) only, as control (b) RB (c) RB + GBIB:AOT (80:20) and (d) RB + GBIB:AOT (20:80).